PAPER

Check for updates

Predicting image quality degradation as a result of two-phase sample transport in LA-ICP-TOFMS mapping of carbon-based materials†

Johannes T. van Elteren, [ID] *a Tom Van Helden, [ID] b Dino Metarapi, [ID] a Thibaut Van Acker, [ID] *b Kristina Mervič,a Martin Šala [ID] a and Frank Vanhaecke [ID] b

Recent findings reported by Van Helden *et al.* (*Anal. Chim. Acta*, 2024, **1287**, 342089) have revealed that a whole suite of elements (S, Zn, As, Se, Cd, I, Te and Hg) undergoes two-phase sample transport during mapping of carbon-based materials using nanosecond laser ablation (LA) combined with an ICP-mass spectrometer equipped with a quadrupole or time-of-flight analyzer (ICP-QMS or ICP-TOFMS). Examining single pulse response (SPR) profiles, it became evident that these elements are transported in both gaseous and particulate forms. This phenomenon leads to notable widening of the SPR profiles, exhibiting two peaks in which the distribution of the ablated sample material across the peaks depends on the laser fluence. Consequently, the image quality may degrade, especially at higher pixel acquisition rates typically used with low-dispersion ablation cells. This is experimentally demonstrated by mapping of kidney tissue at low and high pixel acquisition rates and including elements which show one-phase (Mg, Ca, Fe and Cu) and two-phase (S, Zn, I and Hg) sample transport. To predict the impact of sample transport phenomena on the image quality through modeling, well-established computational models were utilized for virtual LA-ICP-MS mapping of a phantom and incorporate the experimentally obtained element-specific SPR profiles referenced in the aforementioned work. Downloadable interactive Python-based software for MS Windows was developed to study the effect of mapping parameters on the image quality, which was quantified by the structural similarity index (SSIM).

Introduction

LA-ICP-TOFMS has become a widely used analytical technique for the elemental analysis of solid samples in many scientific disciplines, including geology, biology, forensics, medicine, and archaeology.[1–4] The bottleneck in LA-ICP-MS analysis is often related to quantification of biomaterials, with significant attention given to calibration in elemental mapping.[5–7] However, a largely unrecognized issue in LA-ICP-MS mapping of soft biological tissues is the bimodal transport of certain elements in laser ablation systems.[8,9] While "generic" smearing or lateral blurring caused by overly high scan speeds has been widely discussed in the literature,[10–12] element-specific bimodal

aDepartment of Analytical Chemistry, National Institute of Chemistry, Hajdrihova 19, SI-1000, Ljubljana, Slovenia. E-mail: elteren@ki.si

bDepartment of Chemistry, Atomic & Mass Spectrometry – A&MS Research Group, Ghent University, Campus Sterre, Krijgslaan 281-S12, BE-9000, Ghent, Belgium. E-mail: Thibaut.VanAcker@UGent.be

† Electronic supplementary information (ESI) available: Screen shots (Fig. S1 and S2) of Python-based data processing software for MS Windows (https://github.com/metarapi/Laser-Ablation-Simulation-Tool/releases/latest); experimental demonstration of element-dependent image degradation (Fig. S3). See DOI: https://doi.org/10.1039/d4ja00288a
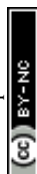
sample transport may further amplify this loss of resolution, yet it has received little focus.

Nanosecond laser ablation-induced generation of gaseous and particulate carbon species from various polymer materials was reported as early as 1998.[13] As elements incorporated in these polymers are mostly associated with the particulate phase, carbon was disqualified as a suitable internal standard for LA-ICP-MS analysis of polymers. Later research confirmed that this is also the case for quantification of elements in other carbon-based materials such as soft biological tissues, and also carbonates, human hair and wood, as the O/C ratio critically influences the amount of gaseous species generated.[14,15] Despite these reported calibration challenges, only recently, it was documented that this two-phase sample transport behavior may also lead to LA-ICP-MS maps with impaired image quality when analyzing soft biological tissues and that higher laser fluences and longer wavelength lasers worsen the degree of gaseous phase formation.[9] Detailed multi-element studies have shown that most elements are transported exclusively in the particulate form, with particle sizes ranging from nanometers to micrometers,[16,17] resulting in narrow and unimodal single-pulse response (SPR) profiles. However, certain elements (such as C, S, Zn, As, Se, Cd, Te, I, and Hg) tend to be transported in both particulate and gaseous forms.[8,18,19] This two-phase element-

specific sample transport results in significantly wider SPR profiles with the second peak of the bimodal SPR attributed to the slower removal of gaseous components, potentially influencing the quality of the elemental maps when non-optimal mapping conditions are chosen.

In particular, in systems with low-dispersion ablation cells,[20,21] this effect will be pronounced when pixel acquisition rates are selected solely on the basis of narrow SPR profiles associated with elements transported in particulate form only, or obtained by ablating non-carbon-based materials such as glass reference materials. This implies that in line scanning mode, pixel information may "spill over" to the next pixel(s), thereby reducing the spatial resolution and causing smear in maps,[22,23] as will be experimentally demonstrated in this work for a number of elements. Fluence has also been shown to affect the amount of material ablated,[19,24,25] thereby influencing image quality due to counting statistics and induced Poisson noise.[26] Furthermore, fluence influences the distribution between the two phases for analyte elements showing bimodal transport.[8] To optimize the pixel acquisition rate and minimize image smear and noise in LA-ICP-TOFMS maps, LA parameters such as repetition rate, lateral scan speed and fluence require optimization. Also, the dosage, referring to the number of partially overlapping laser shots to generate a single pixel, needs to be taken into account.[27,28] Tuning all these settings for multi-element mapping would prove to be labor-intensive in a full experimental context.

To this end, this work allows prediction of the image quality through modeling based on virtual LA-ICP-MS mapping using element- and fluence-related SPR profiles obtained in an earlier work[8] as input. This will allow simulation of the image degradation, whereby the model utilizes earlier developed discrete-time convolution protocols based on two consecutive processes: LA sampling (*via* empirical ablation crater profiles) and aerosol washout/transfer/ICP-MS measurement (*via* experimental SPR profiles).[29,30] The structural similarity index (SSIM),[31,32] a tool used to gauge perceived visual image quality, was employed to quantify image degradation using custom-developed MS Windows software (freely available for download) linked to the experimental element-specific SPR profiles reported earlier.[8]

Experimental

To experimentally demonstrate the potential for image degradation resulting from LA-ICP-TOFMS mapping, kidney tissue was subjected to "slow" and "fast" mapping of eight different elements associated with both unimodal (Mg, Ca, Fe and Cu) and bimodal (S, Zn, I and Hg) transport behaviors. Earlier recorded experimental element- and fluence-specific SPR profiles[8] were used as input for an LA-ICP-TOFMS mapping model to study and predict image degradation. The model was then applied to virtually map an image phantom as a function of concentration, fluence, lateral scan speed, repetition rate, and dosage. SSIM values were compared to gain insights into the optimal mapping settings for achieving the best image quality.

LA-ICP-TOFMS instrumentation

An Iridia LA unit (Teledyne Photon Machines, Bozeman, USA) equipped with a nanosecond 193 nm ArF* excimer-based laser (MLase, Germering, Germany) and a cobalt ablation chamber with a cup-type ablation cell was coupled to an icpTOF 2R time-of-flight based ICP-mass spectrometer (TOFWERK, Thun, Switzerland) *via* the Aerosol Rapid Introduction System (ARIS), comprising the 90 cm long and 1 mm inner diameter PEEK tubing and a co-axial mixing bulb.[23,33] In the mixing bulb, the Ar make-up gas is gently mixed with the He carrier gas that transports the ablated material from the ablation site towards the injector of the ICP-torch. The LA stages are capable of a maximum translation speed of 10 000 μm s^{-1}, while the laser can fire at a maximum repetition rate of 1000 Hz. Daily tuning of the instrument settings was performed while ablating the NIST SRM 612 glass reference material (National Institute of Standards and Technology, Gaithersburg, MA, USA), aiming at high sensitivity across the elemental mass range (based on $^{27}Al^+$, $^{115}In^+$ and $^{238}U^+$), low oxide formation ($^{238}U^{16}O^+/^{238}U^+ <$ 1%), low laser-induced elemental fractionation ($^{238}U^+/^{232}Th^+ \approx$ 1) and low aerosol dispersion (peak width of the $^{238}U^+$ signal < 10 ms).

Samples

Gelatin standards for SPR profiling and quantification purposes. Earlier recorded SPR profiles were obtained by firing a single laser pulse at a gelatinous droplet (as a proxy for soft biological tissues) spiked with a multi-element standard to a concentration $C_{gel}(i)$ of 100 μg g^{-1} (after oven-drying). The droplet standard was regarded as "thick", *i.e.*, even with a dosage of 10, the laser did not ablate completely through the droplet. The standard contained 25 elements and was prepared following established procedures.[8,34]

Kidney tissue. Kidney tissue was collected from an earlier cisplatin nephrotoxicity study in Cynomolgus monkeys.[35] All animal procedures were performed in accordance with the Guidelines for Care and Use of Laboratory Animals of WuXi AppTec Test Facility (AAALAC accredited, Suzhou, China) and approved by the Animal Ethics Committee of the Test Facility (Institutional Animal Care and Use Committee, IACUC). Tissue sections of 5 μm thickness were deposited on SuperFrost glass microscope slides, deparaffinized and stained with hematoxylin and eosin. Calibration was performed based on quantitative ablation of the samples and multi-element spiked gelatin micro-droplet standards, as described by Schweikert et al.[36]

LA-ICP-TOFMS analysis

Demonstration on kidney tissue. Elemental mapping of kidney tissue was performed utilizing a 15 μm diameter circular laser beam, a laser fluence of 0.6 J cm^{-2} and a dosage of 5, ensuring quantitative and selective ablation of the entire tissue section.[37] Pixel acquisition rates selected were 10 and 100 pixels per s, associated with repetition rates of 50 and 500 Hz and scan speeds of 150 and 1500 μm s^{-1}. The number of mass spectra summed was 217 and 2173 for 100 and 10 pixels per s,

This journal is © The Royal Society of Chemistry 2025

J. Anal. At. Spectrom., 2025, **40**, 520–528 | **521**

respectively, resulting in integration times of *ca.* 10 and 100 ms. Although quantitative measurements (in μg g^{-1}) were prioritized, the gelatin standards did not contain all the elements of interest so that qualitative measurements (in counts) are also reported. Mapping was performed on two locations of the kidney tissue, close to the edge and including tubule structures, by monitoring the entire mass spectrum. A total of eight nuclides (Mg-24, S-32, Ca-44, Fe-56, Cu-65, Zn-66, I-127 and Hg-202) was selected for further processing.

Recording of SPR profiles. As reported earlier,[8] line scanning was conducted on the gelatinous material utilizing a 20 μm diameter circular laser beam, 30 laser fluences in the range 0.07–6.30 J cm^{-2}, and a low laser repetition rate of 1 Hz to facilitate the recording of individual SPR profiles. The integration time of the icpTOF 2R was set to 3 ms, integrating 65 full elemental mass spectra (collected every 46 μs). For every fluence used, the profiles were constructed by averaging the results obtained upon firing 100 laser pulses onto the pristine sample surface. Relevant recorded data can be viewed in the downloadable software (SPR Profiles, ESI†). Most nuclides display narrow peak profiles, indicating sample transport primarily associated with particulate phase washout. However, for certain elements (S, Zn, As, Se, Cd, Te, and I) much wider double peaks are observed as a result of two-phase sample transport involving an additional gaseous phase. Two-phase sample transport also exhibits a correlation with fluence: generally, the gaseous peak decreases with a lower fluence, while the particulate peak increases. By reducing the laser fluence, the degree of gaseous phase formation can be decreased but cannot be fully eliminated, thereby affecting the image quality.

Numerical calculations and data processing

Simulations were performed in MATLAB R2020a (MathWorks, Portola Valley, CA, USA), and for visualization of the data Origin software (Origin 2018, OriginLab Corporation, Northampton, MA) and ImageJ 1.49 (ref. 38) (National Institutes of Health (NIH), Bethesda, MD, USA) were used. Software was developed using the Python programming language, utilizing Custom-Tkinter to create an interactive and user-friendly graphical interface, and allowing users to interact with the software easily. Additionally, it employs Matplotlib to generate and display a wide range of plots and graphs, providing extensive visualization and plotting capabilities for SPR profiles and image degradation, next to calculation of the SSIM (for details, see Fig. S1 and S2, ESI†).

Results and discussion

Demonstrating element-specific image degradation *via* LA-ICP-TOFMS mapping of kidney tissue

From Fig. S3,† it is evident that LA-ICP-TOFMS mapping of kidney tissue results in varying degrees of image degradation for different elements and scan speeds. Although structural features are limited, except for Fe, the tubules through which primary urine flows serve as good indicators of resolution loss, displaying artifacts in the form of smearing. "Slow" scanning

results in negligible differences in smearing, as evidenced by the very similar appearances of the tubules across all elements. In contrast, "fast" scanning reveals less sharp presentations of the tubules for S, Zn, I, and Hg, while the ones for Mg, Ca, Fe, and Cu are depicted with much higher resolution. Moreover, the overall tissue presentation for the first set of elements appears more "blurry" compared to the second set. This proves that one has to be careful to fully appreciate the benefits of ultrafast LA-ICP-TOFMS mapping, as it may compromise the resolution for certain elements, particularly those associated with SPR profiles exhibiting bimodal transport.[8] To gain deeper insights into image degradation during ultrafast LA-ICP-TOFMS mapping and to optimize operational parameters (repetition rate, lateral scan speed, dosage and fluence), a model was developed based on a virtual LA-ICP-TOFMS mapping approach. This approach utilized experimentally obtained element-specific SPR profiles as a function of fluence, as described below.
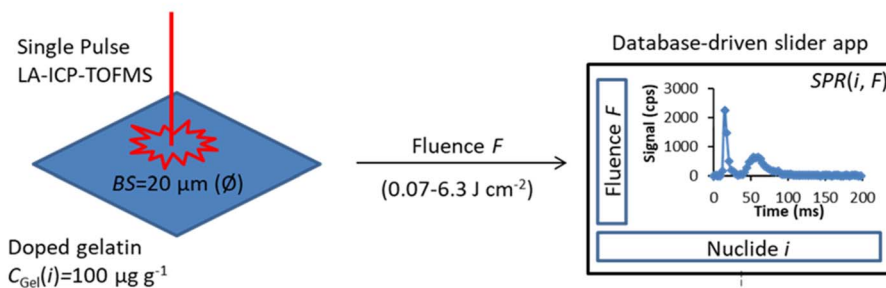
Model development

Fig. 1 provides a schematic layout of the modeling approach based on experimental element-specific SPR profiles as a function of fluence (SPR Profiles, ESI†) as input for the model. This requires that the same laser beam size (20 μm, circular) and fluence (0.07–6.30 J cm^{-2}) are used in the model. The model simulates the LA-ICP-TOFMS mapping procedures (SPR Image Quality, ESI†), and it was performed following earlier developed computational protocols[27,29,30,32] on a phantom (image of a Johannes Vermeer painting, "Girl with a Pearl Earring", *ca.* 1665, Wikimedia Commons, cropped and resized to 3000 × 3000 square pixels, each pixel having a dimension of 1 μm × 1 μm). The 8 bit phantom image (256 grayscale values; black = 0 and white = 255) was regarded as a "gelatinous sample" with maximum concentrations $C_{\text{Phant}}(i)$ in the range of 10–1000 μg g^{-1} for each of the nuclides i and having the same ablation characteristics as the gelatinous droplet standard described above.

To computationally perform mapping, we used numerical calculations based on consecutive convolution functions in the time domain ($\otimes$ = mathematical convolution operator) to define unidirectional sampling blur (1), directional washout smear (2), augmented by introduction of Flicker and Poisson noise (3):

(1) Blurred image = phantom $\otimes$ BS, where BS was simulated by a beam of 20 μm diameter with a super-Gaussian order 10, *i.e.*, somewhere in-between a flat-top profile and a true Gaussian profile.[39] As convolution was performed in discrete steps of 1 μm, one can select how the image was sampled, *i.e.*, by selecting each 20th step in both horizontal and vertical directions, true spot-resolved mapping (dosage $D = 1$) was performed. By selecting, *e.g.*, each 2nd step in the horizontal direction and each 20th step in the vertical direction, oversampling was performed with a dosage D of 20/2 = 10. Oversampling implies that the sample information recorded originated from an elongated area up to *ca.* 40 × 20 μm^2, thereby causing a slight amount of additional sampling blur but much higher sensitivity.

522 | *J. Anal. At. Spectrom.*, 2025, **40**, 520–528

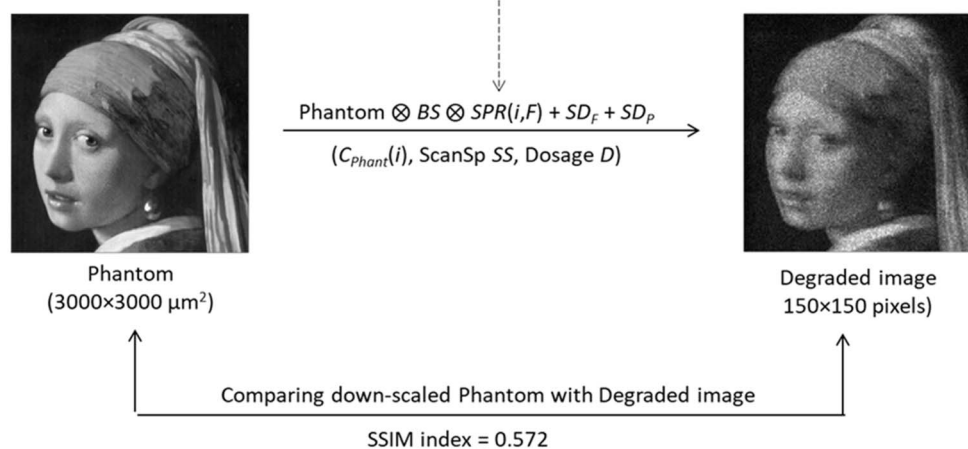This journal is © The Royal Society of Chemistry 2025

Fig. 1 Overview of the modeling approach to predict the image quality in LA-ICP-TOFMS mapping (ESI†).

(2) Smeared image = blurred image $\otimes$ SPR(i,F), where SPR(i,F) is the element-specific single pulse response, expressed in cps, for a specific element i at a laser fluence F. Depending on the selected lateral scan speed SS (μm s^{-1}), repetition rate RR (Hz) and dosage D, the SPR(i,F) may blur the image when the SS is too high and the sample aerosol mixes with that from the next laser shot(s). This happens when the width of the SPR(i,F) profile, defined as the full width at 1% of the maximum intensity (FW0.01M, s), exceeds the interval between laser pulses, $i.e.$, when FW0.01M > D/RR = BS/SS (for generation of square pixels). The signal intensity A (counts) accumulated per pixel in the smeared image has been corrected by taking into account the selected sample concentration $C_{\text{Phant}}(i)$.[30]

(3) The degraded image in Fig. 1 is the noise-free smeared image to which Flicker noise (SD$_F$ = $q \cdot A/\sqrt{D}$, where $0 \le q \le 1$) and Poisson noise (SD$_P$ = $\sqrt{A}$) have been introduced.[27] The ensuing noise per pixel is RSD = $100 \cdot \sqrt{[\text{SD}_F^2 + \text{SD}_P^2]/A}$ = $100 \cdot \sqrt{[q^2/D + 1/A]}$. We chose to add Flicker noise by selecting a q value of 0.05, which is an experimentally acceptable value.[34] It is evident that increasing the dosage, fluence, and/or concentration reduces image noise by generating more counts per pixel.

To conduct a perceptual image quality comparison using the SSIM, the original phantom was downscaled to match the size of the degraded image using 20×20 average block sampling. As the degraded image has undergone a translation in the scan direction, registration of the images was performed before computation of the SSIM (values between 0 and 1). This index, which compares the luminance, contrast and structure in the respective down-scaled phantom and degraded images, shows the poor image quality of the degraded image in Fig. 1, as evident from the low SSIM value of 0.572.

Modeled output and visualization of degraded phantom images

The modeling procedure illustrated in Fig. 1 was used to simulate LA-ICP-TOFMS maps for Mg (i = Mg-24) and Zn (i = Zn-66) in the phantom, with a maximum concentration $C_{\text{Phant}}(i)$ of 500 μg g^{-1}. We selected SPR(i,F) profiles associated with fluences F of 0.49 and 4.9 J cm^{-2} and generated virtual LA-ICP-TOFMS maps under four mapping conditions:

(a) Dosage D: 1; fluence F: 4.9 J cm^{-2}; repetition rate RR: 100 Hz; lateral scan speed SS: 2000 μm s^{-1}.

(b) Dosage D: 10; fluence F: 4.9 J cm^{-2}; repetition rate RR: 1000 Hz; lateral scan speed SS: 2000 μm s^{-1}.

(c) Dosage D: 10; fluence F: 0.49 J cm^{-2}; repetition rate RR: 1000 Hz; lateral scan speed SS: 2000 μm s^{-1}.

(d) Dosage D: 10; fluence F: 0.49 J cm^{-2}; repetition rate RR: 250 Hz; lateral scan speed SS: 500 μm s^{-1}.

Mg and Zn were chosen as model elements due to the experimentally confirmed difference in transport behavior (see

Fig. S3†), exhibiting unimodal and bimodal transport, respectively. The behavior of other nuclides is very similar (SPR Profiles, ESI†). The actual impact on image degradation can be evaluated using the developed software (Image Quality, ESI†).

Fig. 2A demonstrates that under spot-resolved single pulse mapping conditions, as in (a), a higher quality map was obtained for Mg compared to Zn. Despite similar sensitivities (11.7 and 11.3 counts in the Mg-24 and Zn-66 SPR(i,F) profiles, respectively), significant smear was introduced in the Zn map due to a bimodal washout process. Although noise levels were high in both maps, increasing the dosage to 10, as in (b), reduced noise significantly. This increased dosage led to lower noise and higher SSIM values for both nuclides. Nevertheless, blur persisted in the Zn map. To mitigate this, the fluence was lowered to 0.49 J cm^{-2}, as in (c), resulting in a significant reduction of the gaseous peak in the Zn-66 SPR profile compared to the fluence of 4.9 J cm^{-2} (Fig. 2B). This indeed improved the image quality of the Zn map, while the image quality of the Mg map slightly decreased due to a lower signal intensity at this lower fluence. By further reducing the pixel acquisition rate to 25 pixels per second, achieved by

lowering the lateral scan speed to 500 μm s^{-1} and the repetition rate to 250 Hz, as in (d), the blur in the Zn map was almost completely eliminated, while the quality of the Mg map remained practically unchanged.

In Fig. 2, we merely scratched the surface in terms of identifying optimal conditions for the best possible image quality in the shortest mapping time. Given the impossibility of showcasing all potential maps under selectable conditions, the next section will delve deeper into using SSIM values for optimization of the image quality.

Prediction of image quality based on SSIM values

To identify the best LA-ICP-TOFMS operating conditions for achieving optimal image quality in the shortest mapping time, we conducted virtual mapping using the modeling approach and extracted SSIM values to evaluate similarity with the original, based on arbitrary but generally accepted metrics:

SSIM > 0.9 indicates excellent quality, 0.7 < SSIM < 0.9 is considered good, 0.5 < SSIM < 0.7 fair, and SSIM < 0.5 poor.
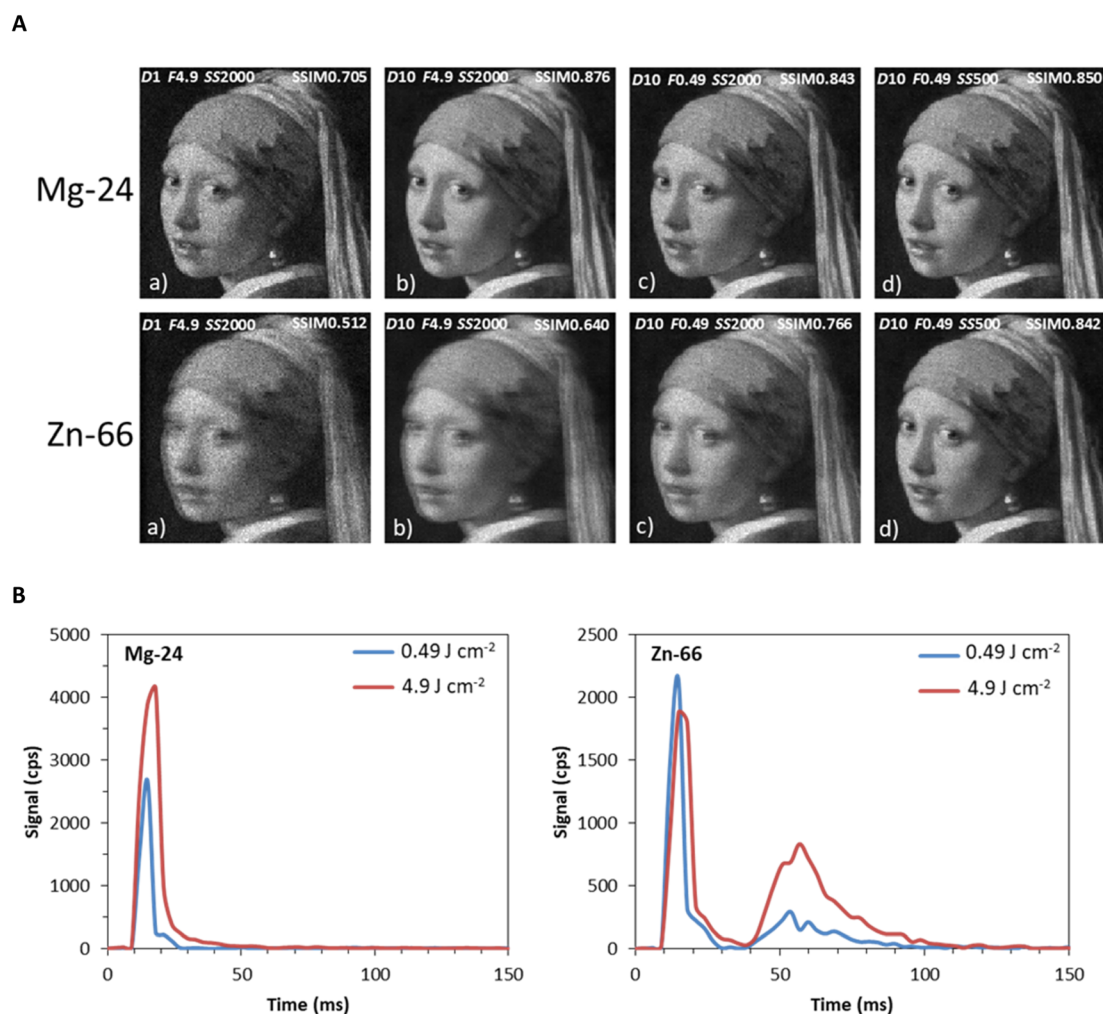

Fig. 2 Displayed are maps associated with virtual LA-ICP-TOFMS mapping of Mg-24 and Zn-66 in the phantom image under mapping conditions a, b, c, and d (A), along with SPR profiles for fluences of 0.49 and 4.9 J cm^{-2} (B). The peaks around 15 and 60 ms are associated with the particulate and gaseous phase, respectively.

524 | *J. Anal. At. Spectrom.*, 2025, **40**, 520–528

This journal is © The Royal Society of Chemistry 2025

SSIM values were represented in color maps, correlating them with fluence (30 conditions) and lateral scan speed (20 conditions), considering 3 concentrations and 2 dosages for the 2 model nuclides selected. This produced six color maps for each nuclide, derived from a total of 3600 variables used in the SSIM calculations for each nuclide. Mapping conditions were constrained by the maximum repetition rate of the laser (1000 Hz) and the maximum lateral scan speed of the stage (10 000 μm s^{-1}) using the formula SS = (BS·RR)/D. Therefore, for dosages of 1 and 10, repetition rates and lateral scan speeds were limited to 500 Hz/10 000 μm s^{-1} and 1000 Hz/2000 μm s^{-1}, respectively.

However, to facilitate easier comparison, the lateral scan speed was restricted to a maximum of 2000 μm s^{-1}, thereby limiting the repetition rates to 100 and 1000 Hz for dosages of 1

and 10, respectively. For smaller beam diameters, higher repetition rates and lateral scan speeds are possible. Fig. 4A (Mg-24) and B (Zn-66) summarize the simulation findings, illustrating differences in the image quality between the two nuclides that can be attributed to distinct sample transport phenomena. While higher concentrations and dosages generally enhance the overall image quality by reducing Poisson noise, detailed analysis of individual sub-graphs in Fig. 3 presents a more intricate picture.

Variations in fluence and lateral scan speed have distinct effects on Mg and Zn maps. For a specific dosage–concentration pair, Mg maps are minimally affected by these parameters, despite a slight tailing and an increased sensitivity of the unimodal SPR profiles at higher fluences (Mg, SPR Profiles,
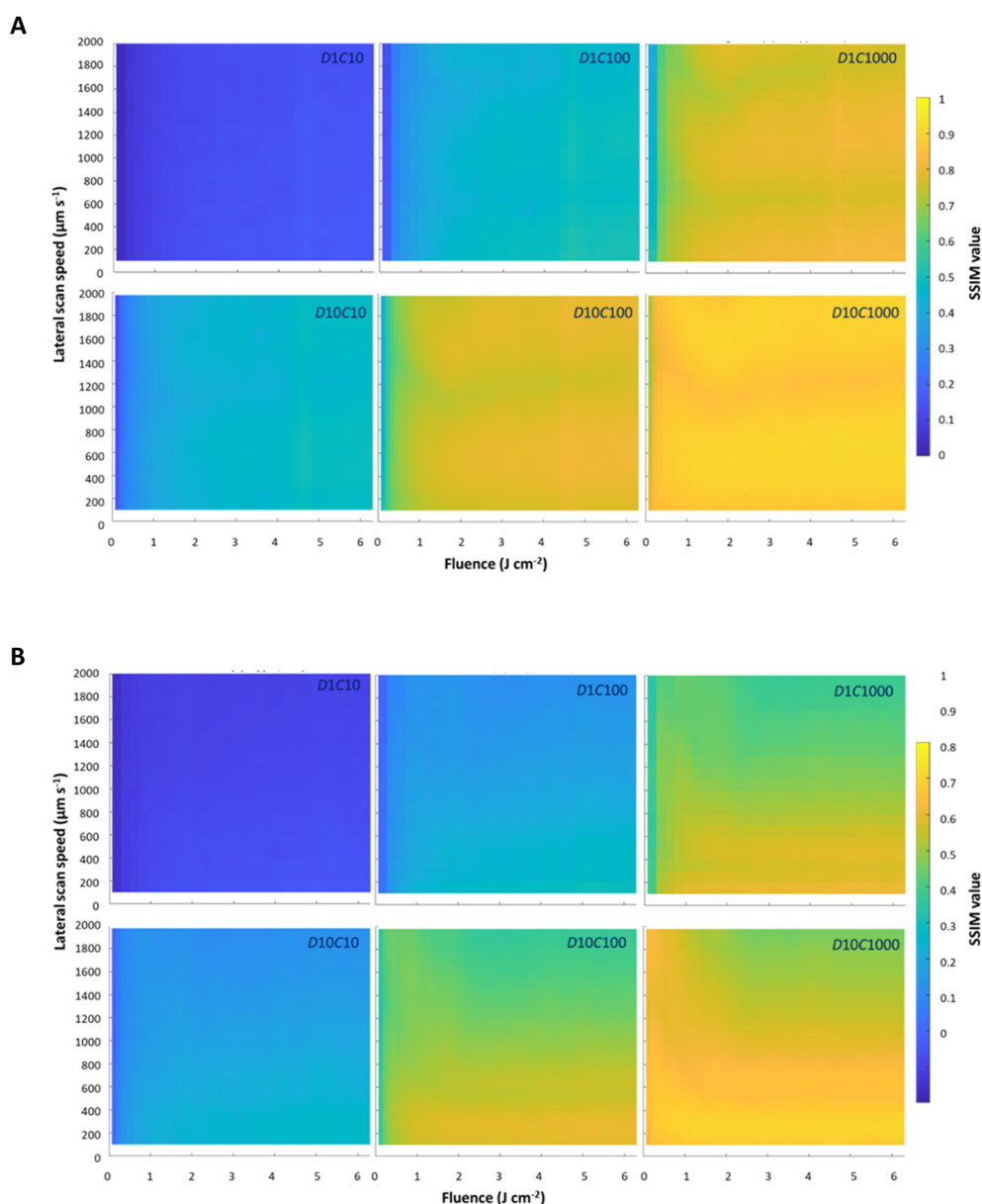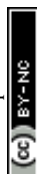

Fig. 3 SSIM values following virtual LA-ICP-TOFMS mapping of Mg-24 (A) and Zn-66 (B) in the phantom, considering 3 concentrations and 2 dosages, plotted against fluence and lateral scan speed.

This journal is © The Royal Society of Chemistry 2025

J. Anal. At. Spectrom., 2025, **40**, 520–528 | **525**

ESI†). As depicted in Fig. 3A, image degradation for Mg remains negligible at higher fluences, even at elevated lateral scan speeds. In contrast, the Zn maps in Fig. 3B are significantly affected by changes in the lateral scan speed and/or fluence, in particular for higher dosages and/or concentrations. Zn SPR profiles demonstrate a marked fluence dependency (Zn, SPR Profiles, ESI†), with the peak ratios in the bimodal SPR profiles shifting in response to fluence changes. At lower fluences, the gaseous peak diminishes, while the particulate peak is enhanced, allowing the particulate peak to dominate and improve the image quality.[8] From Fig. 3B, it can be seen that image degradation for Zn becomes more pronounced with increasing fluence and/or lateral scan speed at higher dosage–concentration pairs.

Detailed mapping conditions related to optimal image quality

To aid comprehension of the information presented in Fig. 3, we isolated the SSIM values corresponding to fluences of 0.49 and 4.9 J cm^{-2} (see Fig. 4) and a lateral scan speed of 2000 μm s^{-1} (see Fig. 5).

Fig. 4 displays the results constrained by fluence, revealing that the image quality for Mg-24 is minimally influenced by the lateral scan speed, while fluence exerts a significant impact. This is evident from the comparison of SSIM values at both fluences, which shows that a higher fluence generally results in improved image quality. This improvement can be attributed to reduced Poisson noise due to the approximately 2.5-fold increase in the amount of material ablated. For Zn-66, the situation differs, as image quality is significantly affected by the
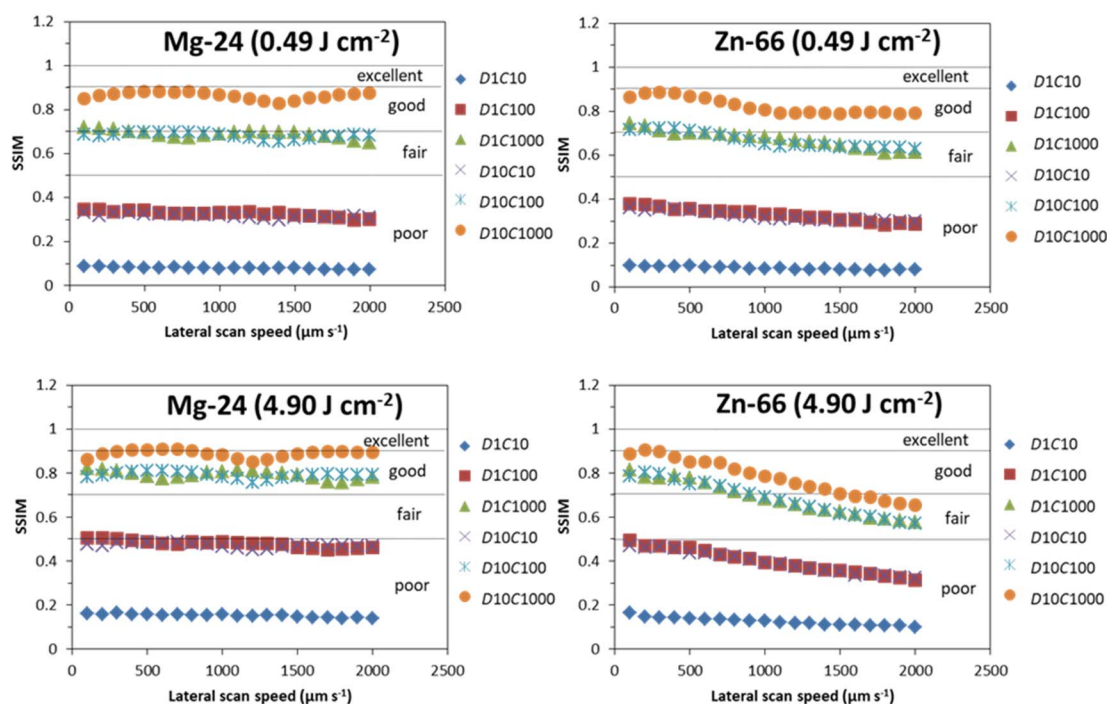

Fig. 4 SSIM values as a function of the lateral scan speed for Mg-24 and Zn-66 at fluences of 0.49 and 4.9 J cm^{-2}. These values are extracted from Fig. 3 and are accompanied by the depiction of image quality criteria.
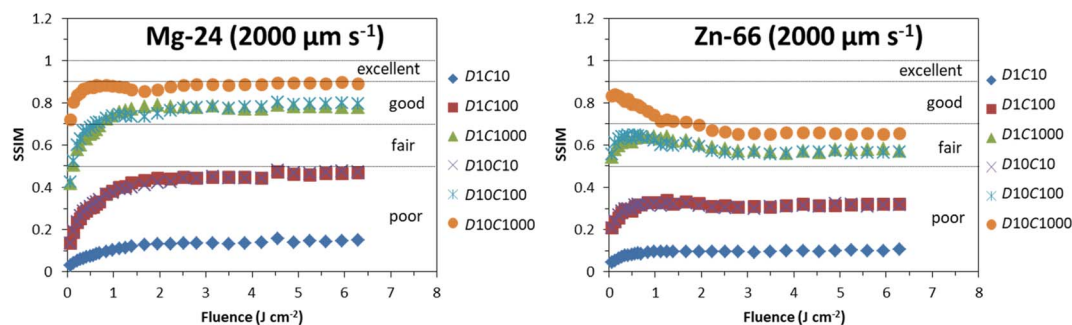

Fig. 5 SSIM values as a function of the fluence for Mg-24 and Zn-66 at a lateral scan speed of 2000 μm s^{-1}. These values are extracted from Fig. 3 and are accompanied by the depiction of image quality criteria.

526 | J. Anal. At. Spectrom., 2025, **40**, 520–528

This journal is © The Royal Society of Chemistry 2025

lateral scan speed, in particular for higher dosages and concentrations at a fluence of 4.9 J cm^{-2}. This follows from the decrease in the particulate-to-gaseous peak ratio in the SPR profile, which drops from 3.9 to 1.3 as the fluence increases from 0.49 to 4.9 J cm^{-2}. Consequently, the Zn map becomes more susceptible to smearing because the gaseous peak becomes dominant, increasing the likelihood of forming a "shadow image" at higher lateral scan speeds. Another significant observation regarding image quality from Fig. 5 is that, for both nuclides, increasing the dosage by ten-fold produced the same effect as measuring a sample with a concentration that is ten times higher. Specifically, increasing the dosage from 1 to 10 effectively mitigates the noise associated with a concentration decrease from 100 to 10 μg g^{-1} or from 1000 to 100 μg g^{-1}.

Generation of high-quality multi-elemental maps also requires careful optimization of the fluence. Fig. 5 presents the results constrained by a lateral scan speed of 2000 μm s^{-1}, demonstrating that the image quality for Mg-24 progressively improves with increasing fluence for all concentration and dosage conditions, reaching a plateau at approximately 4 J cm^{-2}. Conversely, for Zn-66, the image quality peaks around a fluence of 0.5 J cm^{-2} or lower, particularly when sufficient counts are generated to achieve fair or better image quality. Identifying an optimal fluence that maximizes the image quality for both Mg-24 and Zn-66 simultaneously at a scan speed of 2000 μm s^{-1} is challenging due to their contradictive requirements. The best approach is to find a compromise fluence that is effective for both nuclides, based on SSIM values and image quality criteria, or use a fluence that is optimal for only one of the nuclides. When working with thin sections of biological tissues, the fluence should be selected below the ablation threshold of the glass substrate (typically < 0.5 J cm^{-2}) to avoid signal contribution originating from co-ablation of the underlying glass substrate.

For other nuclides, the downloadable software offers interactive experimentation with mapping conditions to study changes in the virtually mapped phantom. By considering the unique transport behaviors of these nuclides and taking into account their fluence-affected SPR profiles, the software can be used to get insight into the effect of mapping conditions on the image quality.

Conclusions

In this work, we demonstrate that ultrafast LA-ICP-TOFMS mapping of carbon-based materials can lead to element-dependent image degradation, as observed in the mapping of eight elements in kidney tissue. Structural tissue features showed resolution loss for S, Zn, I, and Hg, while no losses were noted for Mg, Ca, Fe, and Cu. To gain deeper insights into resolution loss in LA-ICP-TOFMS maps under varying mapping conditions, image quality was predicted using a modeling procedure achieved by virtually mapping a multi-element-doped gelatinous phantom. This procedure utilizes experimental SPR profiles in conjunction with computational convolution protocols to generate a degraded output. Image

degradation was calculated based on parameters such as element concentration, fluence, lateral scan speed, repetition rate, and dosage, influencing both sampling blur and transport smear as well as system and measurement noise. SSIM algorithms were employed to verify the quality of the output.

Proponents of one- and two-phase sample transport selected for this study were Mg-24 and Zn-66, respectively. The findings indicate that the small group of elements that exhibit two-phase sample transport (S, Zn, As, Se, Cd, I, Te and Hg) presents challenges with regard to ultrafast mapping with high image quality. This is because these elements are transported in both gaseous and particulate forms, unlike most other elements which are transported only in particulate form. This two-phase transport can lead to smear in the element maps if the operational conditions are not finely tuned.

While efforts may be made to enhance the sample transport efficiency through adjustments such as the increasing carrier gas flow or reducing interface length, the reality remains that only a limited range of system options are at our disposal to address two-phase sample transport. This limitation becomes particularly frustrating when measuring multiple elements that require simultaneous handling of both one- and two-phase sample transport phenomena. Consequently, maximizing the image quality must rely on adjusting the operational LA-ICP-TOFMS mapping parameters.

The modeling procedure revealed that higher dosages and/or element concentrations improved the image quality for both Mg-24 and Zn-66 through better counting statistics, effectively reducing Poisson noise. Furthermore, Mg-24 maps showed minimal sensitivity to lateral scan speeds up to 2000 μm s^{-1}, but higher fluences led to a higher amount of ablated material and improved image quality. The image quality of Zn-66 maps was significantly affected by both the lateral scan speed and fluence, with image quality benefiting from lower lateral scan speeds and specific fluence ranges. Because two-phase sample transport leads to much wider SPR profiles, Zn maps are more susceptible to image smear than Mg maps with regard to the lateral scan speed. Additionally, the particulate-to-gaseous peak ratio in the Zn-66 SPR profile is heavily influenced by fluence; lower fluences result in a higher ratio and thus a more dominant particulate peak. Therefore, fluences below 0.5 J cm^{-2} are favored for maximizing the image quality in Zn-66 maps.

In summary, obtaining high-quality images in the shortest mapping time with LA-ICP-TOFMS necessitates careful optimization of the mapping conditions, a process that can be effectively explored using the modeling approach outlined here. The interactive Python software developed for this purpose allows users to virtually experiment with mapping conditions based on experimental SPR profiles specific to our LA-ICP-TOFMS system, derived from ablation of multi-element-doped gelatin standards. It offers valuable insights into how mapping conditions may affect image quality for elements exhibiting unimodal or bimodal transport.

This journal is © The Royal Society of Chemistry 2025

J. Anal. At. Spectrom., 2025, 40, 520–528 | 527

Data availability

The data supporting this article have been included as part of the ESI.†

Conflicts of interest

There are no conflicts to declare.

Acknowledgements

References

1 D. Chew, K. Drost, J. H. Marsh and J. A. Petrus, *Chem. Geol.*, 2021, **559**, 119917.

2 P. A. Doble, R. Gonzalez De Vega, D. P. Bishop, D. J. Hare and D. Clases, *Chem. Rev.*, 2021, **121**, 11769–11822.

3 D. Pozebon, G. L. Scheffler, V. L. Dressler and M. A. G. Nunes, *J. Anal. At. Spectrom.*, 2014, **29**, 2204–2228.

4 T. Trejos, R. Koons, P. Weis, S. Becker, T. Berman, C. Dalpe, M. Duecking, J. Buscaglia, T. Eckert-Lumsdon, T. Ernst, C. Hanlon, A. Heydon, K. Mooney, R. Nelson, K. Olsson, E. Schenk, C. Palenik, E. C. Pollock, D. Rudell, S. Ryland, A. Tarifa, M. Valadez, A. van Es, V. Zdanowicz and J. Almirall, *J. Anal. At. Spectrom.*, 2013, **28**, 1270–1282.

5 H. Pan, L. Feng, Y. Lu, Y. Han, J. Xiong and H. Li, *TrAC, Trends Anal. Chem.*, 2022, **156**, 116710.

6 A. Limbeck, P. Galler, M. Bonta, G. Bauer, W. Nischkauer and F. Vanhaecke, *Anal. Bioanal. Chem.*, 2015, **407**, 6593–6617.

7 K. Mervič, M. Šala and S. Theiner, *TrAC, Trends Anal. Chem.*, 2024, **172**, 117574.

8 T. Van Helden, K. Mervič, I. Nemet, J. T. van Elteren, F. Vanhaecke, S. Rončević, M. Šala and T. Van Acker, *Anal. Chim. Acta*, 2024, **1287**, 342089.

9 T. Van Helden, S. Braeuer, T. Van Acker, O. Leroux, D. Van Der Straeten and F. Vanhaecke, *J. Anal. At. Spectrom.*, 2022, **37**, 1455–1461.

10 M. Bonta, A. Limbeck, C. D. Quarles Jr, D. Oropeza, R. E. Russo and J. J. Gonzalez, *J. Anal. At. Spectrom.*, 2015, **30**, 1809–1815.

11 M. T. Westerhausen, D. P. Bishop, A. Dowd, J. Wanagat, N. Cole and P. A. Doble, *Anal. Chem.*, 2019, **91**, 14879–14886.

12 P. Bohleber, M. Roman, M. Šala and C. Barbante, *J. Anal. At. Spectrom.*, 2020, **35**, 2204–2212.

13 J. L. Todolí and J. M. Mermet, *Spectrochim. Acta, Part B*, 1998, **53**, 1645–1656.

14 D. A. Frick and D. Günther, *J. Anal. At. Spectrom.*, 2012, **27**, 1294–1303.

15 D. A. Frick, C. Giesen, T. Hemmerle, B. Bodenmiller and D. Günther, *J. Anal. At. Spectrom.*, 2015, **30**, 254–259.

16 J. Koch, A. Von Bohlen, R. Hergenröder and K. Niemax, *J. Anal. At. Spectrom.*, 2004, **19**, 267–272.

17 H.-R. Kuhn, J. Koch, R. Hergenröder, K. Niemax, M. Kalberer and D. Günther, *J. Anal. At. Spectrom.*, 2005, **20**, 894–900.

18 T. Van Acker, A. Rua-ibarz, F. Vanhaecke and E. Bolea-fernandez, *Anal. Chem.*, 2023, **95**, 18579–18586.

19 A. Jerše, K. Mervič, J. T. van Elteren, V. S. Šelih and M. Šala, *Analyst*, 2022, 5293–5299.

20 S. J. M. Van Malderen, A. J. Managh, B. L. Sharp and F. Vanhaecke, *J. Anal. At. Spectrom.*, 2016, **31**, 423–439.

21 O. B. Bauer, O. Hachmöller, O. Borovinskaya, M. Sperling, H. J. Schurek, G. Ciarimboli and U. Karst, *J. Anal. At. Spectrom.*, 2019, **34**, 694–701.

22 M. Šala, V. S. Šelih, C. C. Stremtan and J. T. Van Elteren, *J. Anal. At. Spectrom.*, 2020, **35**, 1827–1831.

23 T. Van Acker, S. J. M. Van Malderen, T. Van Helden, C. Stremtan, M. Šala, J. T. Van Elteren and F. Vanhaecke, *J. Anal. At. Spectrom.*, 2021, **36**, 1201–1209.

24 R. Srinivasan and B. Braren, *Chem. Rev.*, 1989, **89**, 1303–1316.

25 I. Horn and D. Günther, *Appl. Surf. Sci.*, 2003, **207**, 144–157.

26 M. Burger, G. Schwarz, A. Gundlach-Graham, D. Käser, B. Hattendorf and D. Günther, *J. Anal. At. Spectrom.*, 2017, **32**, 1946–1959.

27 J. T. van Elteren, M. Šala and D. Metarapi, *Talanta*, 2021, **235**, 122785.

28 C. Neff, P. Keresztes Schmidt, P. S. Garofalo, G. Schwarz and D. Günther, *J. Anal. At. Spectrom.*, 2020, **35**, 2255–2266.

29 J. T. van Elteren, A. Izmer, V. S. Šelih and F. Vanhaecke, *Anal. Chem.*, 2016, **88**, 7413–7420.

30 J. T. van Elteren, V. S. Šelih and M. Šala, *J. Anal. At. Spectrom.*, 2019, **34**, 1919–1931.

31 Z. Wang, A. C. Bovik, H. R. Sheikh and E. P. Simoncelli, *IEEE Trans. Image Process.*, 2004, **13**, 600–612.

32 J. T. van Elteren, M. Šala and V. S. Šelih, *Anal. Chem.*, 2018, **90**, 5916–5922.

33 S. J. M. Van Malderen, T. Van Acker and F. Vanhaecke, *Anal. Chem.*, 2020, **92**, 5756–5764.

34 M. Šala, V. S. Šelih and J. T. van Elteren, *Analyst*, 2017, **142**, 3356–3359.

35 T. Van Acker, S. J. M. Van Malderen, M. Van Heerden, J. E. McDuffie, F. Cuyckens and F. Vanhaecke, *Anal. Chim. Acta*, 2016, **945**, 23–30.

36 A. Schweikert, S. Theiner, D. Wernitznig, A. Schoeberl, M. Schaier, S. Neumayer, B. K. Keppler and G. Koellensperger, *Anal. Bioanal. Chem.*, 2022, **414**, 485–495.

37 T. VanAcker, S. J. M. Van Malderen, L. Colina-Vegas, R. K. Ramachandran and F. Vanhaecke, *J. Anal. At. Spectrom.*, 2019, **34**, 1957–1964.

38 C. A. Schneider, W. S. Rasband and K. W. Eliceiri, *Nat. Methods*, 2012, **9**, 671–675.

39 J. T. van Elteren, D. Metarapi, K. Mervič and M. Šala, *Anal. Chem.*, 2023, **95**, 9863–9871.

528 | *J. Anal. At. Spectrom.*, 2025, **40**, 520–528

This journal is © The Royal Society of Chemistry 2025